ORIGINAL RESEARCH ARTICLE

A Melt Pool Temperature Model in Laser Powder Bed Fabricated CM247LC Ni Superalloy to Rationalize Crack Formation and Microstructural Inhomogeneities

DI WANG, SHENG LI, GUOWEI DENG, YANG LIU, and MOATAZ M. ATTALLAH

This study of the laser powder bed fusion (LPBF) of γ'-strengthened Ni superalloy CM247LC focuses on the development of a melt pool temperature model to predict crack density within the alloy. This study also analyzes spatter and elemental evaporation, which might cause defects and inhomogeneities, at different melt pool temperatures. The melt pool temperature model provides more accurate predictions than the widely used energy density model. Spatter particles were collected and characterized to study their sizes and chemical compositions, compared with the virgin powder, recycled powder, and as-built samples, to probe the impact of their entrapment into the melt pool. This study also investigated Al evaporation, revealing that its extent does not correlate with the laser energy density and is believed to be rather limited by comparing the chemistry of the virgin powder and the build. Last, the impact of LPBF process parameters on the formation of these inhomogeneities, and accordingly crack formation, was studied using finite element analysis by estimating the maximum melt pool temperature and correlating it with the formation of the microstructural inhomogeneities. The morphology of the various cracking modes was associated with the process parameters.

https://doi.org/10.1007/s11661-021-06457-5
© The Author(s) 2021

I. INTRODUCTION AND LITERATURE REVIEW

NICKEL superalloys have been widely used for critical components in extreme conditions due to their excellent high-temperature strength, fatigue life, good creep performance, and oxidation resistance,[1] with γ'-strengthened cast alloys being used within high-temperature aeroengine sections due to their superior performances.[2] MAR-M247 is a γ'-strengthened, directionally solidified Ni superalloy, which has been used in turbine blades. CM247LC, a chemically modified version of MAR-M247, has reduced C content, lower impurities, and improved grain boundary strength in comparison. This shows superior high-temperature strength and good creep life attributed to the high volume fraction of γ'.[3] The processability of CM247LC using additive manufacturing, especially laser powder bed fusion (LPBF), has been the subject of several investigations. CM247LC shows poor weldability and is susceptible to postweld reheat cracking due to the high γ' fraction,[4] in addition to solidification cracking with dendritic morphology within the high heat input conditions.[5] Todd[6] explained the solidification crack formation mechanism considering the strain theory, whereby the residual liquid confines to channels between the dendrites as solidification proceeds, forming a liquid film. Localized contractions of the solid then cause cavities to form within the liquid film, generating "hot tear" cracks. These defects can propagate under thermal residual stress.[7] Besides the solidification cracking, there is associated grain boundary cracking with the formation of a liquid film along a grain boundary, opening a crack under the influence of the thermal residual stresses during cooling.[8] Due to the reheating and remelting associated with LPBF, ductility dip cracking (DDC)[9] could occur, associated with the poor ductility of Ni superalloys at intermediate temperature ranges, resulting in crack formations under the action of the residual stresses. Crack formation occurs due to metallurgical and process-induced factors.[10] Carter *et al.*[11] used process parameter optimization to reduce

DI WANG is with the School of Mechanical and Automotive Engineering, South China University of Technology, Guangzhou 510640, P.R. China and also with the School of Metallurgy and Materials, University of Birmingham, Birmingham B152TT, UK. SHENG LI and MOATAZ M. ATTALLAH are with the School of Metallurgy and Materials, University of Birmingham. Contact e-mail: M.M.Attallah@bham.ac.uk; s.li.2@bham.ac.uk GUOWEI DENG is with the School of Mechanical and Automotive Engineering, South China University of Technology. YANG LIU is with the Faculty of Mechanical Engineering and Mechanics, Ningbo University, Ningbo 315211, China.

Manuscript submitted March 28, 2021, accepted September 9, 2021. Article published online October 5, 2021

Table I. Chemical Composition of As-Supplied CM247LC Powder Compared With the Nominal Content (Weight Percent)

Content	C	Cr	Ni	Co	Mo	W	Ta	Ti	Al	Hf
Nominal	0.07	8	bal.	9	0.5	10	3.2	0.7	5.6	1.4
Measured	0.066	8.1	bal.	9.22	0.49	10.3	3.32	0.72	5.8	1.4

cracking density and porosity, as high laser energy density caused "jagged" solidification cracks with an obvious dendritic morphology to form, whereas low laser energy density caused grain boundary cracks.

Conversely, the microstructural inhomogeneity caused by evaporation in LPBF of Ni superalloys and its negative effect on the mechanical properties have not provoked significant attention. Juechter *et al.*[12] investigated the evaporation phenomena and found the extent of evaporation to be linearly proportional to the energy input, which strongly depends on laser power and scanning speeds. Besides the energy density, the composition of the alloy could also affect the occurrence of evaporation, including its content and by-products. In CM247LC, Al possesses the lowest boiling point (2447 °C) and a higher vapor pressure than other elements, making it the most likely to evaporate during LPBF. This may also relate the keyholing effect to evaporation, generating evaporated by-products, which would condense quickly due to the low temperatures within the build chamber, compared with those within the melt pool.[13] The condensed spatter would be entrapped, either within the powder bed or the melt pool, leading to microstructural/chemical inhomogeneity within the form of microsegregation, and potentially cracking.[9]

Studies on spatter focused on process modeling,[14] characterization,[15] and parametric studies, investigating the factors that control spatter.[16] As spatter will fall back into the powder bed, or get entrapped within the melt pool, subsequently remelting and resolidifying, studies have investigated the impact of the contaminated powder on the microstructure and properties of LPBF parts.[17] O'Leary *et al.* investigated the recyclability of Ti-6Al-4V powder on the mechanical properties,[18] while Tang *et al.*[19] examined the influence of repeated powder recycling on the characteristics of the Ti–6Al–4V powder, including powder composition, particle size distribution, apparent density, flowability, and particle morphology. Similar studies on Ni superalloys are lacking and are timely to perform.

This study focuses on the influence of spatter and elemental evaporation on microstructural inhomogeneity in LPBF-processed Ni superalloy CM247LC and the subsequent microsegregation and cracking. This study combines the use of process modeling and microstructural characterization to correlate the formation of inhomogeneities with the process parameters and the crack formation mechanisms.

II. MATERIALS AND METHODS

Argon gas atomized CM247LC spherical powder within the size range 15 to 53 μm was supplied by LPW Technology (Runcorn, United Kingdom). Table I shows the chemical composition of the as-received powder, measured using inductively coupled plasma (ICP), *vs* the nominal composition.

A. *Laser Powder Bed Fusion*

The CM247LC samples were manufactured using a range of parameters on a Concept Laser*M2 Cusing system without heated bed (400 W maximum laser power, 4200 mm/s maximum scan speed), operated in a controlled argon atmosphere of 0.1 pct O_2, with a fixed layer thickness of 30 μm. The system uses a Gaussian laser beam of ~ 70- to 80-μm diameter. The samples were built using a raster (simple) scanning strategy, with 90 deg rotation between the subsequent layers within the "meander-on" mode, where the laser beam stays on when the laser slows, prior to changing the scan direction, and with a corner delay (the time the laser beam stops moving when changing direction) of 0.08 ms. This study built cubic $10 \times 10 \times 10$ mm^3 samples on an IN718 substrate, with the cubes rotated 45 deg regarding the powder recoating direction. The experiment used four levels of laser power (100, 175, 250, and 350 W), four levels of scanning speed (800, 1375, 2400, and 4000 mm/s), and four levels of scan/hatch spacing (0.045, 0.0525, 0.0675, and 0.12 mm). The energy density model with its three variants,[20] namely, the linear energy density ($E_L = p/v$), the area energy density ($E_A = p/v/h$), and the volumetric energy density ($E_V = p/v/h/t$), where p is laser power (W), v is scanning speed (mm/s), h is hatch spacing (mm), and t is layer thickness (mm), were used to study the impact of the process parameters. The samples were sectioned in both the XY and YZ planes perpendicular to the laser scanning vector (X, Y), where Z is the build direction.

*Concept Laser is a trademark of Concept Laser GmbH, Lichtenfels, Germany.

B. *Thermal Modeling*

ANSYS was used to calculate the highest temperature experienced within the melt pool, per the model described by Liu *et al.*[21] The model uses a substrate of dimensions $4 \times 2 \times 1$ mm^3 covered by a single layer of powder. The powder layer was finely meshed by the SOLID70 hexahedral element, with dimensions of $0.015 \times 0.015 \times 0.015$ mm^3. To reduce the computational time, the substrate, finely meshed near the powder layer, was coarsely meshed away from the

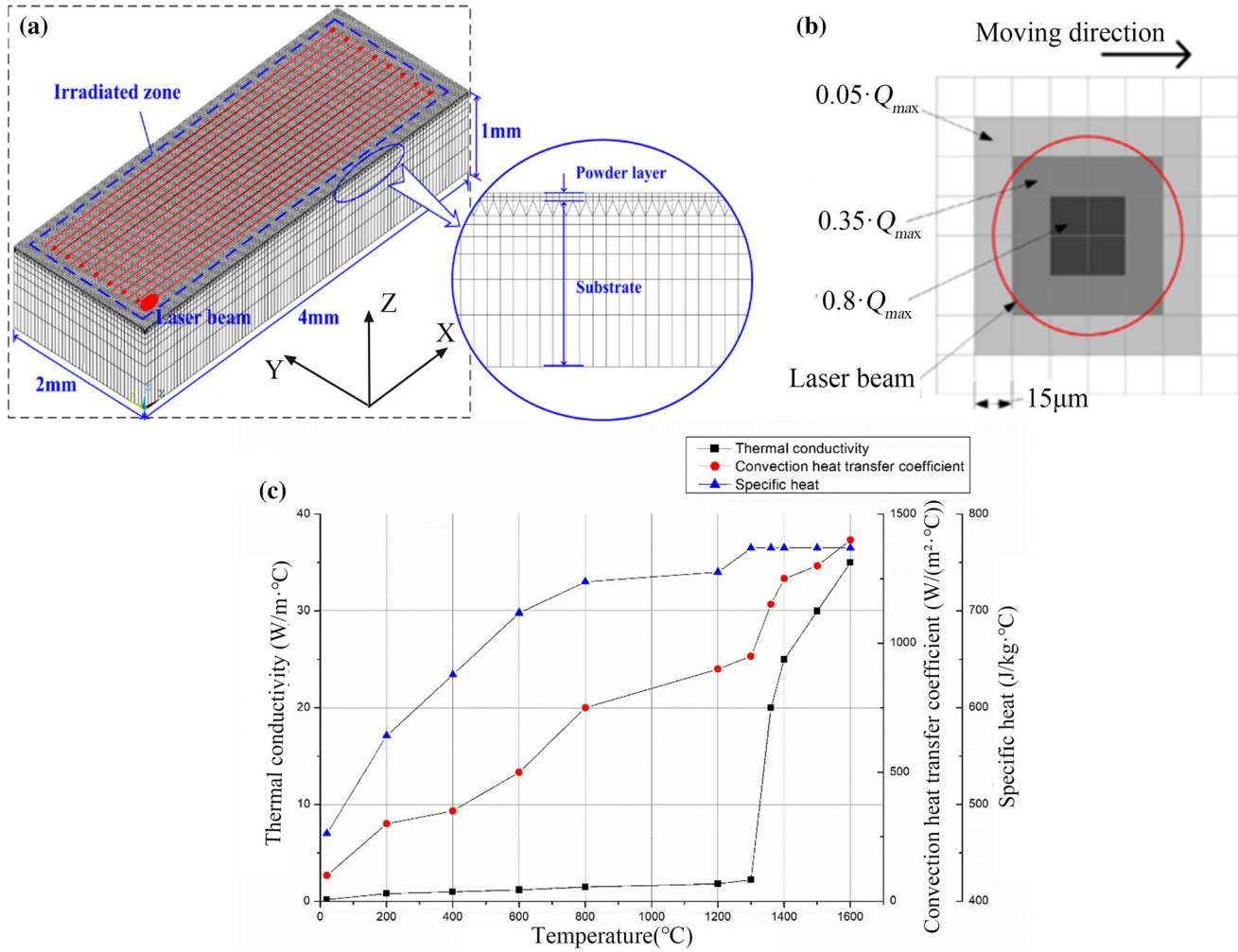

Fig. 1—Maximum temperature FE model for CM247LC LPBF, showing (*a*) the model and meshing of the laser-irradiated area and substrate, (*b*) the mesh for the Gaussian heat source, and (*c*) material parameters for the FE model.

laser-irradiated area, as shown in Figure 1. This study adopted a Gaussian heat source to describe the laser beam source, whereby the laser energy irradiated the powder bed within the form of thermal flux, which can be defined as

$$Q = \frac{2AP}{\pi R^2} \exp\left(\frac{-2r^2}{R^2}\right) \quad [1]$$

where A is the absorption of the powder material, taken as 0.55[22,23]; P is the laser power, and R is the laser beam radius, taken as 0.05 mm. The Gaussian heat source is moved along the X-axis with a raster zigzag pattern, as shown in Figure 1(a). To consider convection,[24] this study applied the surface effect unit SURF152 on the powder bed surface. The finite element (FE) model of the Gaussian heat source is shown in Figure 1(b), where 6 × 6 elements cover the area equal to the circus area of the laser beam and the coefficients of heat flux loaded onto elements (irradiated area) are assigned as 0.8, 0.35, and 0.05, respectively. Figure 1(c) shows the thermophysical parameters (thermal conductivity, convection, and specific heat) of CM247LC powder[25] used in this model.

Among the thermophysical properties of powder materials, thermal conductivity plays the most important role in the heat and transfer process during the LPBF process. The effective thermal conductivity is calculated by the Sih model[26] when the temperature is lower than the solidus temperature T_S. As the temperature falls into the range of T_S to T_M (melting temperature), the effective thermal conductivity is calculated by an empirical formula proposed by Shen *et al.*[27] When the temperature exceeds the T_M, the effective thermal conductivity is assigned to a constant of about 35 W/m °C, which takes the fluid flow within the molten pool into account.

In this work, the calculated temperature drop caused by the thermal convection and radiation was less than 150 °C, indicating that the thermal convection and radiation exerted have a weak influence on the temperature in the molten pool. The same conclusion was also reported by Hussein *et al.*[24]

$$\begin{cases} k_e = k_g\left[(1-\sqrt{(1-\varphi)})\left(1+\frac{\varphi k_r}{k_g}\right) \right. \\ \left. + \sqrt{1-\varphi}\left(\frac{2}{1-\frac{k_g}{k_S}}\left(\frac{1}{1-\frac{k_g}{k_S}}\ln\left(\frac{k_S}{k_g}\right)-1\right)+\frac{k_r}{k_g}\right)\right] \\ T < T_S k_e = k_g(T) + \rho_r(T)^4\left(k_S(T)-k_g(T)\right) \\ T_S \le T < T_M k_e = 35 \quad T > T_M \end{cases} \quad [2]$$

The accuracy of the numerical model has been verified in one of the author's works, which compared the width of melting tracks obtained by numerical and experimental methods.[21]

C. *Microstructural Characterization*

To study the evaporation and spatter formation, this study collected spatter particles from the LPBF chamber; a carbon tap was stuck on the upwind side of the recoater (downwind side of the substrate) to collect spatter particles blown by argon circulation. The as-received and recycled powders, as well as spatter particles, were mounted, ground, and polished to reveal the internal microstructure. For this, Zeiss optical, Hitachi TM3000,** and JEOL† 7000 scanning electron microscopes, fitted with backscattered electron (BSE) and energy dispersive X-ray spectroscopy (EDX) detectors, were used. Samples were then etched to reveal the microstructure in Kalling's reagent (2 g $CuCl_2$, 50 g HCl, and 50 g C_2H_5OH).

This study then used image analysis to measure the total crack lengths, which helped quantify the cracking density. The investigated area was then subsequently divided to express the cracking density in mm/mm^2. Measurements were performed by averaging six micrographs, covering an examined area of 40,000 μm^2. To accurately explore the Al evaporation mechanism, ICP was used to measure the Al content within the as-built samples.

**Hitachi is a trademark of Hitachi, Tokyo, Japan.

†JEOL is a trademark of JEOL, Tokyo.

III. RESULTS AND DISCUSSION

A. *Microstructural Characterization*

Through analyzing the parametric studies, preliminary optimized parameters of p = 350 W, v = 3000 mm/s, and hatching space h = 0.0675 mm were identified as the parametric combination, showing the least cracking and maximum densification among the investigated parameters. This study investigated the top layer to better understand the formation of defects, melt pool, and microstructure, as the top layer was not affected by remelting or reheating, retaining the as-solidified microstructures, pores, cracks, and imbedded particles/inclusions. Figure 2 shows the microstructure of top layer within the optimum condition. The melt pool depth was ~ 55 μm, almost double the 30-μm nominal layer thickness. The laser energy input results in the penetration and remelting of the previous layer (Figure 2(c)). Microcracks were found around the melt pool boundary (Figure 2(b)). A detailed explanation for crack formation will be discussed in Section II–C.

Interdendritic heterogeneities at the melt pool boundary were found within the optimized sample after etching (Figure 3). Wang *et al.* reported similar inhomogeneous regions[28] within the sample materials and claimed that condensed Al evaporation fell back to the melt pool during the process. EDX analysis was applied to these areas and high Al-Hf content was found in these regions.

B. *Spatter and Its Interaction with the Melt Pool*

Figure 4 shows comparisons between the virgin and recycled powders and the spatter particles. Figures 4(a) and (b) show irregular particles and fine satellites present in virgin powder particles, while Figures 4(c) and (d) show dark contrasting particles in recycled powder and EDX analysis indicates these particles are Al and Hf rich. However, the K_α peak of Al is very close to Hf and the dark contrast in BSE images refers to light elements; hence, these are likely to be Al-rich particles, which is consistent with Wang *et al.*[29] Both virgin and recycled powders have particle sizes ranging between 20 and 60 μm. Figures 4(e) and (f) show the spatter powder collected during the processing, with large particles being around 90 μm and fine particles between 5 and 10 μm. Powders with distinct contrasts were evident in spatter, indicating a different chemical composition in spatter particles. Most Al-rich particles are under 60 μm within the spatter. The presence of Al-rich particles might relate to their selective evaporation during the LPBF process, therefore, chemical analysis was carried out as discussed in Section II–C. The result differs from previous publications[30,31]; in previous experiments on spatter formation through CoCrW alloy, most of the spatter particles were larger than 100 μm.

C. *Microsegregation*

Figure 5 shows EDX mapping on the melt pool *XY* surface (sample surface). It was found that the build had spherical or elongated bulges on the surface that had high Al, Hf, and O content. This was rather unexpected as Hf has a higher vaporization temperature (5200 °C) and a melting point of 2200 °C, which is much higher than Al. Al–Hf segregates due to its partitioning during solidification. This is only clearly visible in the top layers, since the build chemistry gets homogenized by the remelting. However, limited Al-Hf segregation was also observed at the melt pool boundary inside the sample, as shown in Figure 3, which has similar

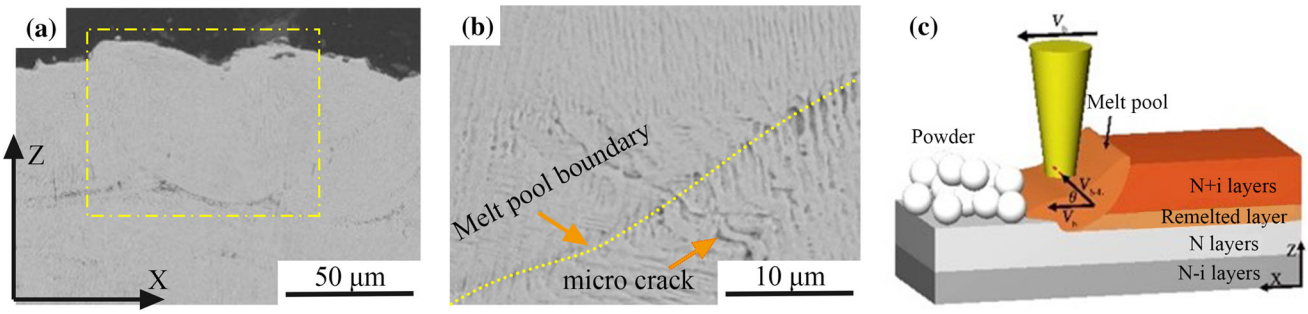

Fig. 2—Backscatter images of top layers of CM247LC LPBF samples: (*a*) the microstructure of the fluctuant surface of the top several layers, (*b*) the microcrack found crossing the melt pool boundary in higher magnification, and (*c*) a sketch of the dendritic growth within the laser-powder interaction zone.

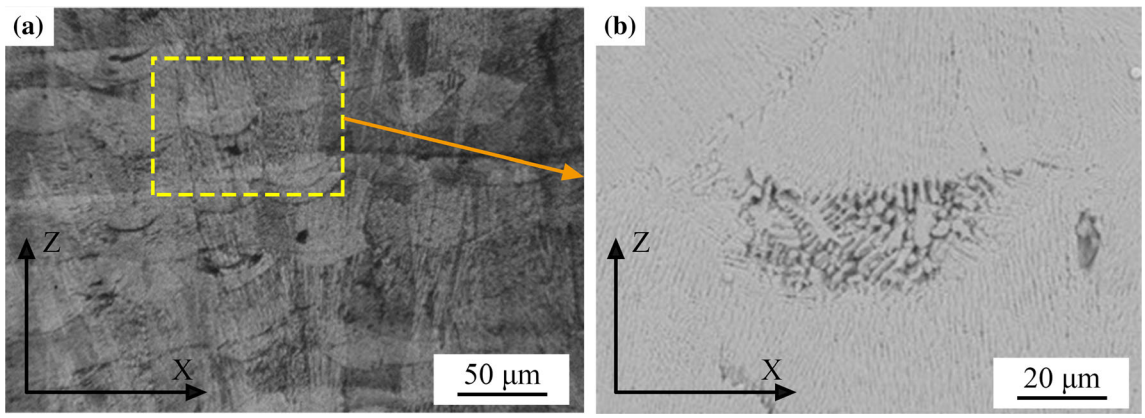

Fig. 3—Microstructure of CM247LC LPBF samples in the XZ section showing (*a*) some defects around the melt pool boundary in optical microscopy after etching; (*b*) the BSE image shows a clear dendritic structure in these defects.

morphology to the cross section of the Al–Hf segregation at the top layer.

Additionally, the Al–Hf segregation shows bright contrast in the BSE image, which differs from the Al-rich particles found in spatter and recycled powder. Therefore, the Al–Hf-rich defects inside the sample could be the unmelt Al–Hf segregation at the melt pool surface. The melt pool in the next layer is perpendicular to the previous layer and there might be insufficient melting at the melt pool boundary, which causes Al–Hf defects inside the sample.

1. *Elemental evaporation*

To investigate evaporation during the process, an analysis of the chemical composition of the powders was conducted. Only limited studies on elemental evaporation have been published until now. The change of the composition caused by elemental evaporation would also affect the properties of the final parts. Usually, the element with low vaporization temperature would be prone to evaporate; in CM247LC alloy, the Al element has a low vaporization temperature of 2470 °C (with a melting point of 660 °C). Spatter collected during the process was compared with virgin and recycled powders and block samples, as shown in Figure 4.

As the elemental evaporation would cause composition variation within the components, Al content within the specimen was further tested through the ICP-IRIS method. This study selected three different parameters to investigate the evaporation and Al content variation within the samples. The peak temperature of the melt pool (°C) is calculated using the model constructed in Section II–B. The Al content testing results are shown in Table III; within the table, the Al content in different parameters varied from 5.58 to 5.66 pct. The laser duration times (defined by spot diameter/scanning speed) for 250 W, 800 mm/s; 400 W, 4000 mm/s; and 175 W, 1375 mm/s parameters were 125, 25, and 72.7 μs, respectively. Although the Al content in samples deviates from 0.14 to 0.22 pct, the Al-content change has little relation to the energy density or the duration. For example, when E_A is 2.6 J/mm^2, the highest temperature within the melt pool is estimated to be 3080 °C (through ANSYS calculation described in Section II–B) and the laser duration time is 125 μs. However, the Al-content drop is only 0.14 wt pct, which is the least among the three production parameters. An experiment was further carried out to investigate the Al content of recycled powder and spatter particles, with the powder having been reused dozens of times. The Al content within the spatter measured as high as 8.966 pct.

2. *Laser energy density and crack density*

Figure 6 shows the melt pool convection currents, surface topographies, and crack morphologies caused by various linear energy densities ($E_L = p/v$). The melt pool

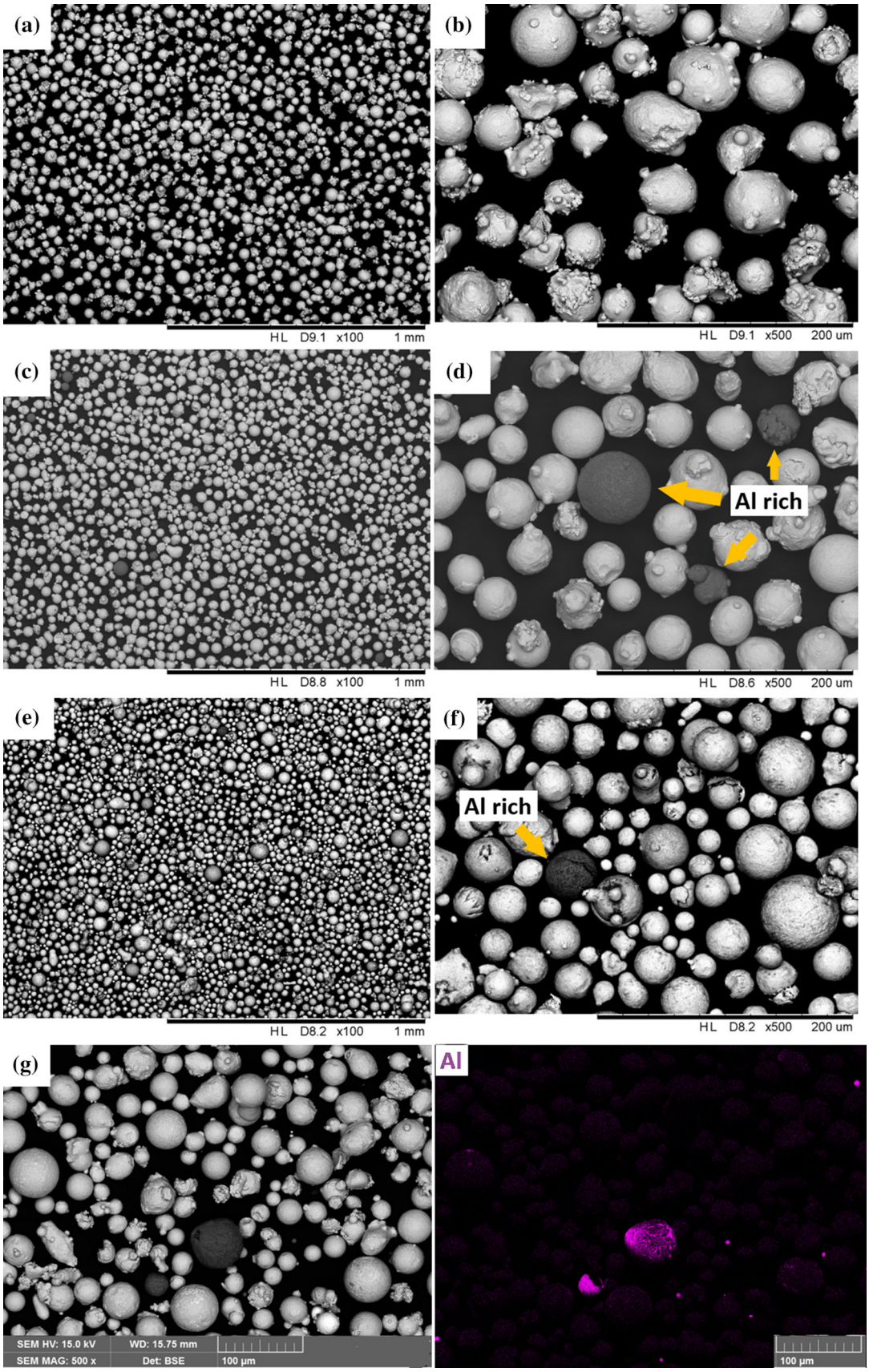
(a)
HL D9.1 x100 1 mm
(b)
HL D9.1 x500 200 um
(c)
HL D8.8 x100 1 mm
(d)
Al rich
HL D8.6 x500 200 um
(e)
HL D8.2 x100 1 mm
(f)
Al rich
HL D8.2 x500 200 um
(g)
SEM HV: 15.0 kV
WD: 15.75 mm
SEM MAG: 500 x
Det: BSE
100 µm
Al
100 µm

◀Fig. 4—Comparison between virgin powder, recycled powder, and spatter particles: (*a*) and (*b*) virgin powder at low and high magnification, (*c*) and (*d*) recycled powder at low and high magnification, (*e*) and (*f*) spatter particles at low and high magnification, and (*g*) BSE images and Al EDX mapping of spatter particles.

weak convection at lower E_L conditions (p/v = 0.04, h = 0.015 mm, and maximum temperature = 1577 °C, as shown in Figure 6(a)-1, uneven surface topography (Figure 6(a)-2), and partial melt microstructure was found in this condition. Although there were no cracks observed, some powder particle boundaries were evident and some powder microstructure was retained

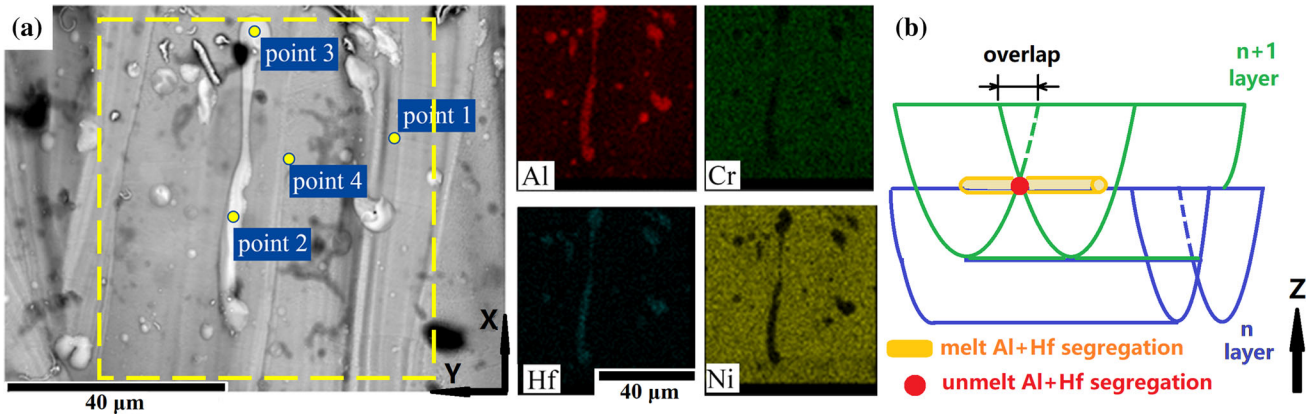

Fig. 5—Analysis of the Al-Hf–rich zone on the XY plane using EDX: (*a*) the BSE image and EDX mapping area (corresponding chemical composition of the indicated points are shown in Table II), (*b*) sketch showing the unmelt Al–Hf segregation between melt pool boundaries.

Table II. Semiquantitative EDX Analysis for the Points in Fig. 5

Wt Pct	C	O	Al	Ti	Cr	Co	Ni	Hf	Ta	W	Total
Point 1	9.72	0.61	5.04	0.64	7.85	8.46	55.90	1.17	2.71	7.89	100
Point 2	6.05	17.12	11.34	0.42	2.44	1.95	13.10	47.59	0	0	100
Point 3	11.05	19.60	12.24	0.41	1.08	1.04	5.57	49.01	0	0	100
Point 4	12.61	0.87	4.23	0.64	7.68	8.52	54.06	1.32	2.30	7.77	100

Table III. Analysis on Al Content (Weight Percent) of the As-Built Laser Powder Bed Fused CM247LC Samples

Processing Parameters	Area Laser Energy Density (J/mm^2)	Highest Temperature (Deg)	Al Content in Virgin Powder (Wt Pct)	Al Content in As-Built Samples (Wt Pct)	Deviation (Pct)
P = 250 W V = 800 mm/s Hatch = 0.12 mm	2.6	3080	5.8	5.66	0.14
P = 400 W V = 4000 mm/s Hatch = 0.0675 mm	1.48	2230	5.8	5.58	0.22
P = 175 W V = 1375 mm/s Hatch = 0.0525 mm	2.43	2200	5.8	5.588	0.212

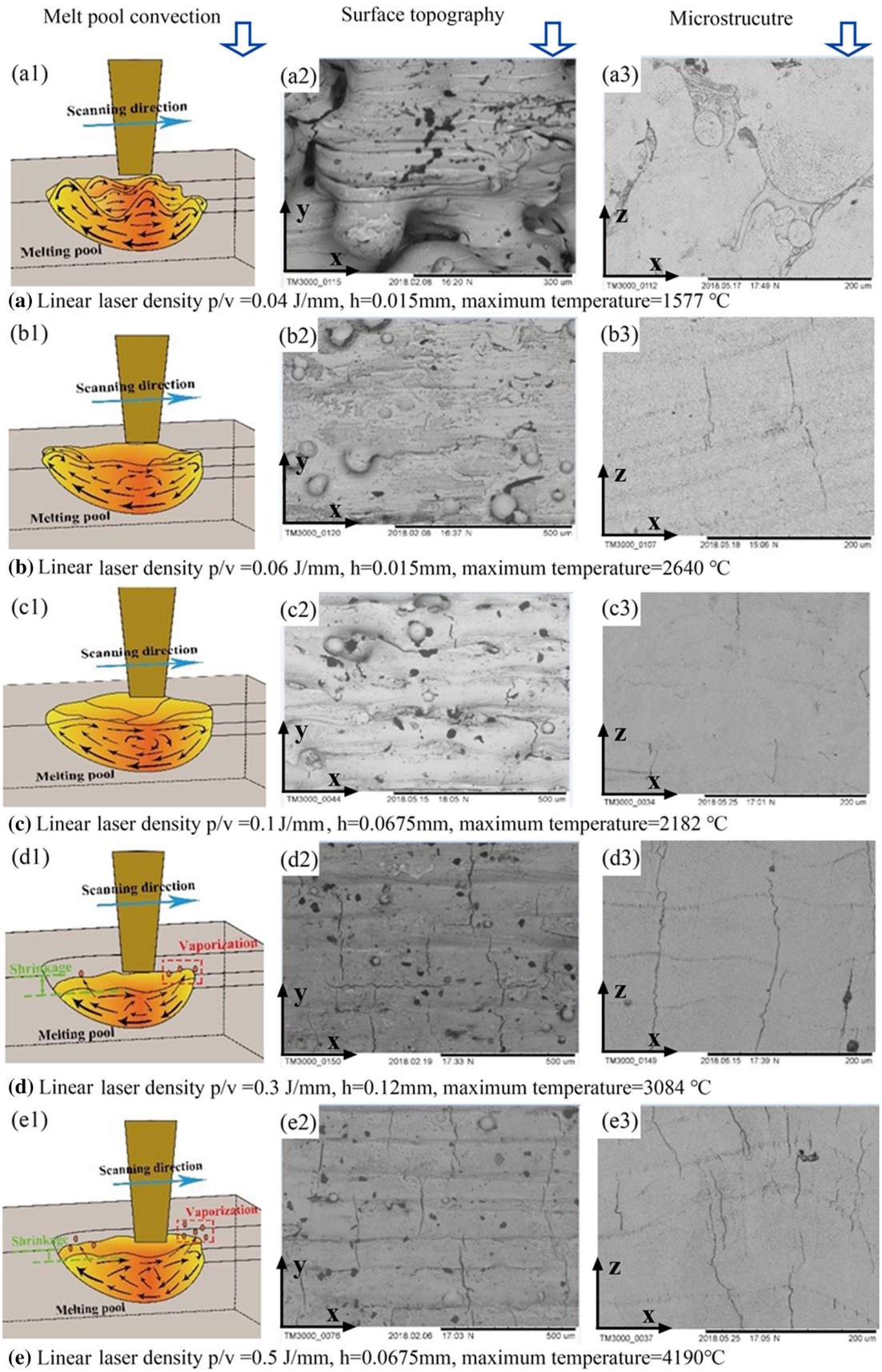

(a) Linear laser density p/v =0.04 J/mm, h=0.015mm, maximum temperature=1577 °C

(b) Linear laser density p/v =0.06 J/mm, h=0.015mm, maximum temperature=2640 °C

(c) Linear laser density p/v =0.1 J/mm, h=0.0675mm, maximum temperature=2182 °C

(d) Linear laser density p/v =0.3 J/mm, h=0.12mm, maximum temperature=3084 °C

(e) Linear laser density p/v =0.5 J/mm, h=0.0675mm, maximum temperature=4190°C

◀Fig. 6—Different melt pool convections (1), surface topographies (2), and crack morphologies (3) caused by various laser energy density: (*a*) 0.04 J/mm linear laser energy density, (*b*) 0.06 J/mm linear laser energy density, (*c*) 0.1 J/mm linear laser energy density, (*d*) 0.3 J/mm linear laser energy density, and (*e*) 0.5 J/mm linear laser energy density.

(Figure 6(a)-3), revealing limited remelting. The remelting usually helps in homogenizing the microstructure. The convection within the melt pool increased with increasing linear energy densities (p/v = 0.06, h = 0.015 mm, and maximum temperature = 2640 °C in Figure 6(b)-1), the surface topography flattened (Figure 6(b)-2), and cracks were found within the *XZ* section (Figure 6(b)-3).[32,33] The cracks were around 200 μm in length, crossing a few layers and parallel to the building direction. The convection within the molten becomes stronger, as linear energy densities further increase (p/v = 0.1, h = 0.0675 mm, and maximum temperature = 2182 °C, as shown in Figure 6(c)-1). This condition results in flat surface topography with track ripples (Figure 6(c)-2). Short microcracks less than 100 μm were found both in the sample surface and *XZ* section (Figure 6(c)-3),the cracks on the surface were perpendicular to the laser scan direction and parallel to the building direction in the *XZ* section. Strong convection within the melt pool and vaporization would happen as linear energy density further increases to p/v = 0.3 (h = 0.12 mm, maximum temperature = 3084 °C, as shown in Figure 6(d)-1). Flat surface and less particles were found on the top surface (Figure 6(d)-2), even though the hatch spacing was larger. However, many cracks around 500 μm in length were found at the surface and the *XZ* section (Figure 6(d)-3). Drastic convection and vaporization (Figure 6(e)-1) occur in the highest linear energy density parameters (p/v = 0.5, h = 0.0675 mm, and maximum temperature = 4190 °C). The surface topography was flat with a small number of particles (Figure 6(e)-2). The cracks remain in the same direction as the lower linear energy density parameters in both the surface and *XZ* section (Figure 6(e)-3), but

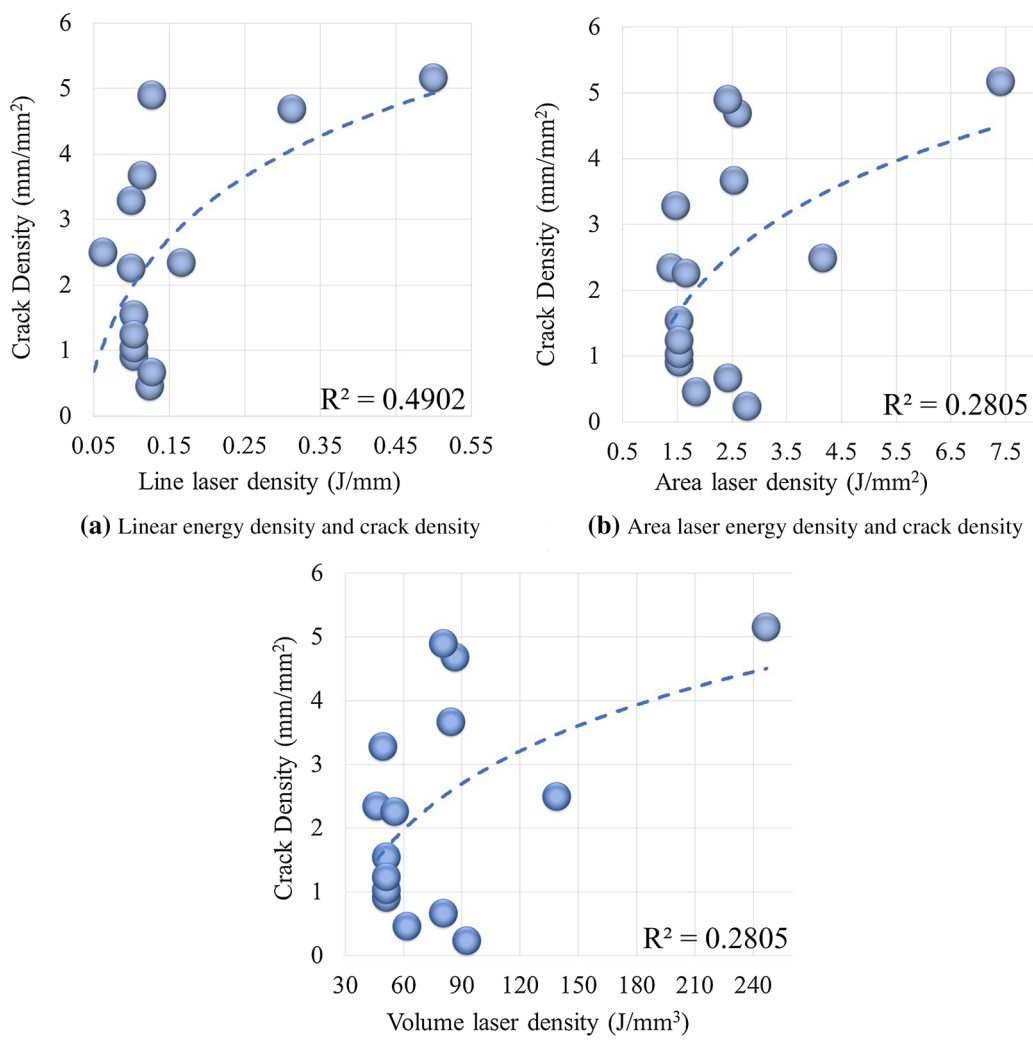

(a) Linear energy density and crack density

(b) Area laser energy density and crack density

(c) Volume laser energy density and crack density

Fig. 7—Correlations between laser energy density models with crack density: (*a*) linear energy density model, (*b*) area energy density model, and (*c*) volume energy density model.

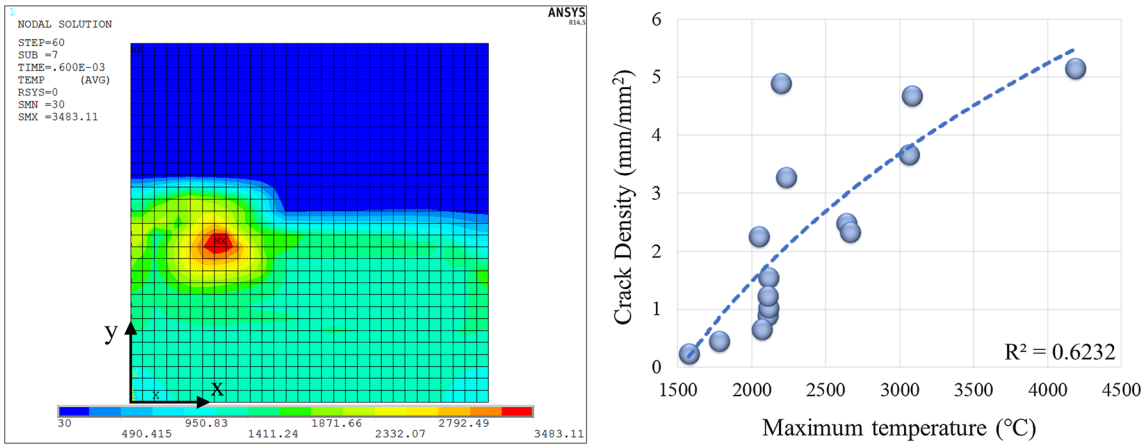

(a) Calculation of the maximum temperature (laser powder 175W, scanning speed 1375mm/s)

(b) Maximum temperature and crack density

Fig. 8—Correlations of the crack density with the maximum temperature: (*a*) modeled temperature contour of the XY section using a 175 W, 1375 mm/s parameter; (*b*) relationship between maximum temperature and crack density.

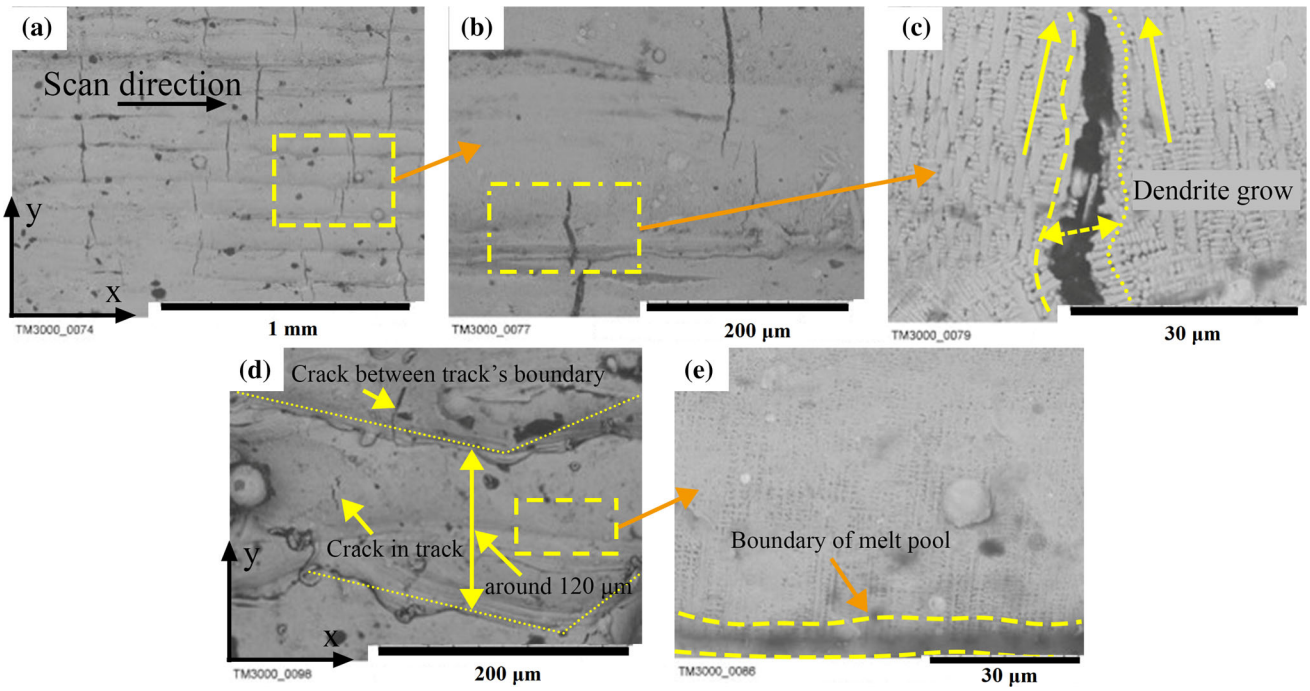

Fig. 9—Crack formation and propagation in the XY plane: (*a*)–(*c*) the crack morphology of high energy density (laser power: 250 W, scanning speed: 800 mm/s); (*d*) and (*e*) the crack morphology of the optimized energy density (laser powder: 350 W, scanning speed: 3500 mm/s).

both the number of cracks and the length of cracks increased, as shown in Figures 6(e)-2 and (e)-3.

Crack density was analyzed to investigate the relation between crack and laser energy densities. A number of fits were attempted to match the relationship trend curves between three different laser energy density models (mm/mm^2). Figure 7 shows correlations between laser energy density with crack density based on different modeling; Figure 7(a) is the relation between linear laser energy density and crack density, Figure 7(b) is the relation between area laser energy density and crack density, and Figure 7(c) is the relation between volume laser energy density and crack density. The results in Figure 7 show that the *R*-squared values for a cubic polynomial fit (the R^2 closer to 1, the trend curves more reliable) were 0.4902, 0.2805, and 0.2805 by using linear laser energy density, area laser energy density, and volume laser energy density, respectively, which indicates the trends were rather weak. The crack density shows no trend with the energy density in Figure 7. Similar results were also reported within the literature when processing various Ni superalloys.[34]

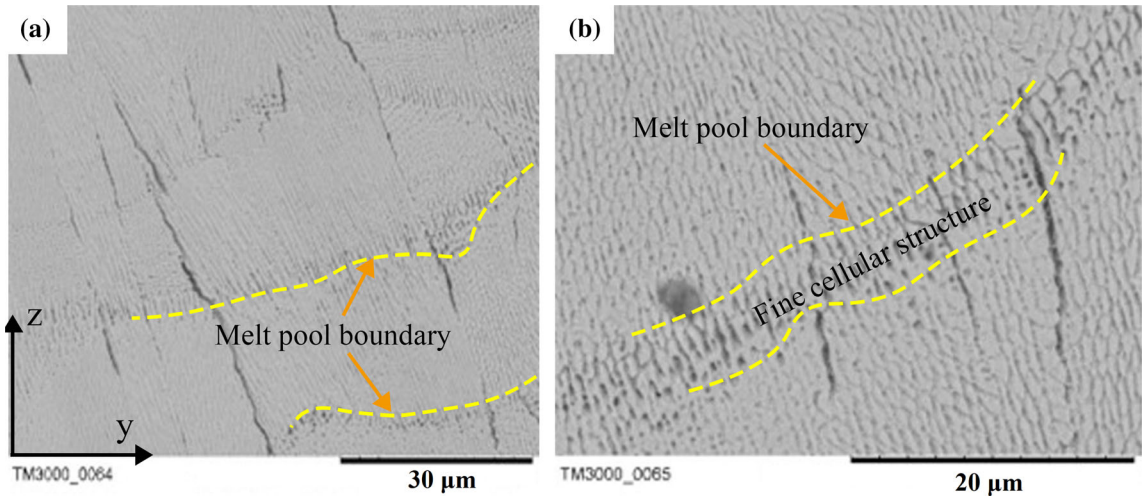

Fig. 10—Crack formation and propagation in the *YZ* section: (*a*) the cracks cross layers and (*b*) the small cracks at the melt pool boundary.

Based on the maximum temperature model discussed in Section II–B, the maximum temperatures for all parameters were calculated. Figure 8(a) shows the top view of the modeled temperature contour in the *XY* section using the 175 W, 1375 mm/s parameter. Figure 8(b) plots the correlation of the crack density with the maximum temperature, showing an increase in cracking density with the increase in maximum build temperature. The trend is more consistent as the R^2 value increases to 0.6232 in the maximum temperature model. Therefore, the maximum temperature within the melt pool could be calculated before selecting parameters to control the porosity or crack. The reason is that the maximum temperature is calculated through modeling the process physics, rather than combining several parameters.

3. *Crack formation and propagating mechanism*

Figure 9 shows crack formation and propagation in the *XY* plane; Figures 9(a) through (c) show the crack morphology of the high energy density sample, which shows the cracks forming perpendicularly to the scan or track direction (Figure 9(a)). Figure 9(c) shows the dendrite growing parallel to the crack propagating direction, and the maximum width of the crack was approximately 5 μm. Figures 9(d) and (e) show the crack morphology on the optimized energy density sample; the cracks were present both within the melt pool and the overlapping zone (melt pool boundary) of two tracks. The crack in Figure 9(d) shows different morphology than that in Figure 9(a), from the aspect of crack dimension and distribution. Figure 9(e) shows a higher magnification image than that chosen in Figure 9(d), where obvious columnar dendrite without cracks was observed. The dendrite nucleates from melt pool boundaries and grows toward the center of the melt pool. The boundary of the melt pool has different microstructures compared with those within the track (Figure 9(e)).

Figure 10 shows the crack formation and propagation in the *XZ* plane; Figures 10(a) and (b) show the crack morphology. From there, the cracks' growth was almost perpendicular to the melt pool boundary and they were parallel to each other. There is a very thin layer of fine cellular structure at the pool boundary (Figure 10(b)). Some microcracks were found at the melt pool boundary cellular structure area (Figure 10(b)), which could develop into macrocracks due to thermal stress.

Based on the analysis of crack formation in *XY* and *XZ* planes, cracks nucleated and propagated between two columnar dendrites and were parallel to the columnar dendrite growing direction. Figure 11 shows two crack-generating mechanisms of CM247LC superalloys observed under optical microscope. The straight cracks shown in Figure 10(a) are ductility dip cracks, which occur because of strain concentration when incoherent precipitates are present together with residual stress. The residual stress will lead to void formations and subsequent cracks will connect a series of voids together. Figures 11(a) and (b) show grain boundary liquation cracking and ductility dip cracking. Figure 11(b) shows dendrite—or solidification—cracks and their formation mechanism. Carter *et al.* also discussed the crack types in laser powder bed fused CM247LC, and they concluded there were two typical cracks: grain boundary and jagged solidification. The boundary crack was due to Al- and Ti-rich phases, which tended to generate cracks and voids due to strain concentration.

D. *Discussion*

The elemental evaporation phenomenon has not raised attention in LPBF; however, it would affect the stability of the process and properties of the parts. The variation of Al content between virgin and recycled powders and bulk samples showed a limited amount of chemistry variation during LPBF processing of CM247LC. The sample, built by high energy input and high melting point parameter, did not present less Al content, according to chemical analysis results. However, the high Al content particles found in spatter

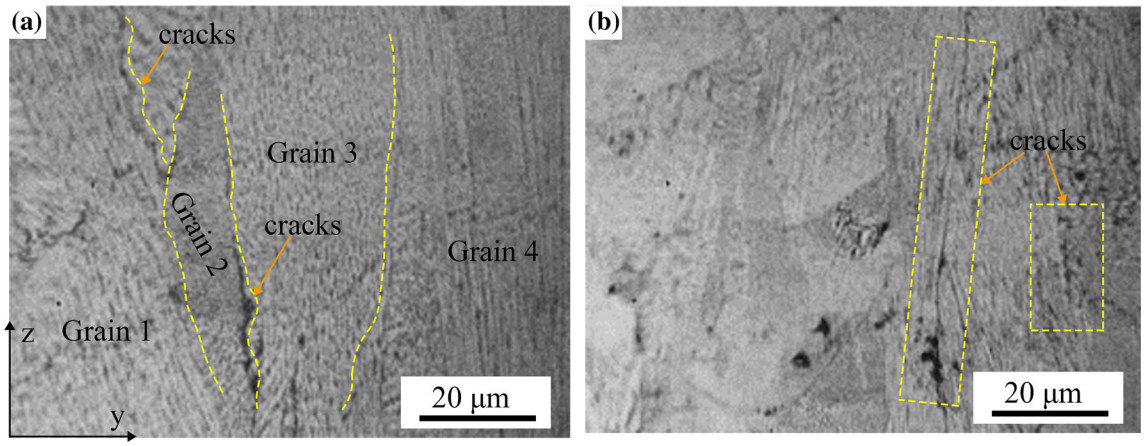

Fig. 11—Two crack-generating mechanisms observed under optical microscope: (*a*) grain boundary cracking and generating mechanism; (*b*) ductility dip cracking and generating mechanism.

and the Al/Hf-rich area within the samples indicate the presence of elemental heterogeneity during the LPBF process.

Although most Al–Hf-rich areas were eliminated by remelting, Figures 3 and 5 show a small portion of Al–Hf-rich phase, indicating a different microstructure than the other parts of the specimen at the melt pool boundary. The Al–Hf concentration caused a heterogeneity microstructure and local chemistry, and may cause cracks to nucleate and propagate, as shown in Figure 11(b). Additionally, the presence of these phases could cause fatal failure at high-temperature applications. Therefore, it is important to relate the Al–Hf-rich phase to the microstructure and properties, and to evaluate if the CM247LC powder composition is suitable for AM. The Al–Hf-rich area might be generated during the melting process in the previous layer (layer *n*), as shown in Figure 5(a); then, the next layer (layer $n + 1$) was perpendicular to layer *n* and the insufficient overlap caused relative low temperature between the melt pool boundaries, as shown in Figure 5(b). Although the melt pool depth was found to be ~ 55 μm, the Al–Hf-rich segregation might remain in the materials due to lower temperature and rapid solidification conditions at the melt pool boundary. Most of the Al–Hf segregation was remelted during the process, but Al evaporation might happen during the remelting and generate Al–Hf-rich spatter. Since the amount of this segregation is small, it is difficult to detect the Al loss *via* chemical test and no obvious Al differences were found between as-built samples. In this case, the Al evaporation from the area without Al–Hf-rich segregation might be very limited. The formation of the Al–Hf-rich region and spatter in LPBF Ni superalloys needs further research. It was found that most Al-rich particles in spatter were under 60 μm; therefore, these particles might not be sieved away during powder recycling. The Al–Hf-rich phases in laser powder bed fused CM247LC superalloys indicate that designing novel superalloys with adjusted low boiling point elements is necessary for AM superalloys.

Defect-free samples are difficult to achieve in LPBF-processed CM247LC. Although no crack was found in the low laser energy density samples (Figure 6(a)-3), the porosity of these samples was too high for structural component application. The higher laser energy density samples, however, tend to crack during the process, leading to poor mechanical properties. Therefore, modeling is commonly used to find the processing window with acceptable porosity and crack density.

Researchers have used different laser energy density models to construct relationships between laser parameters and density, residual stress, and cracks, yet the models failed to accurately provide predictions for the density and cracks of laser powder bed fused CM247LC superalloy, as shown in Figure 7. This might be due to the lack of sensitivity to certain parameters in the porosity and cracks. And the influence of parameters on defects, thermal conditions, and residual stress is different. For example, hatch spacing is a critical parameter, yet how it would affect the density and cracks has not been fully documented; parameters with different hatch spacing could have the same laser energy density and produce samples with almost the same density, yet the difference of accumulated residual stress could be significantly different. Therefore, the maximum temperature model is proposed, based on static parameters and dynamic physical parameters of the material, to improve the accuracy of crack density prediction in Section II–C. In comparison, the experimental results show the crack density increased with increasing melt pool temperature and fit well in the proposed model with R^2 value of 0.6232. This provides a simple but reliable way to predict the crack density of nonweldable materials for the LPBF process.

IV. CONCLUSIONS

In this study, high-density and low-crack CM247LC samples were successfully fabricated using LPBF. A melt pool temperature model has been proposed and applied to optimize the processing parameters for low porosity and crack. The evaporation of Al might introduce Al/Hf-rich particles and cause defects in as-fabricated materials.

1. The microstructural characteristics of laser powder bed fused CM247LC were analyzed from the top layers; the solidification front grows parallel to the maximum thermal gradient and normal to the solid/liquid interface within the melt pool, and grains of laser powder bed fused microstructure also grow epitaxially along the solidification interface.
2. The unique Al–Hf-rich phases were found both on the sample surface and within the sample near the melt pool boundary. This phase was correlated with Al–Hf-rich particles found in spatter and was one of the reasons for cracking in laser powder bed fused CM247LC superalloys. It suggests Al–Hf composition should be controlled when developing novel Ni superalloy for AM.
3. This study found fine particles around 10 μm and large particles around 90 μm with distinct contrast in spatter powder and recycled powder using BSE imaging. Chemical analysis showed a slight chemistry difference between virgin powder and the built samples. Therefore, no strong evidence indicates the evaporation of Al during LPBF. The formation of epitaxy defects and spatter needs further research.
4. The two different cracking mechanisms in the as-built CM247LC alloy were observed and analyzed, including grain boundary cracks and an in-grain solidification crack. Maximum temperatures were calculated and correlated with the crack density. Comparison to the energy density model proved the maximum melt pool temperature model was more accurate when predicting the crack density. This model could also be used for parameter optimization of nonweldable alloys.

ACKNOWLEDGMENTS

One of the authors (DW) thanks the China Scholarship Council for the award to study for 1 year at the University of Birmingham (Grant No. 201706155082).

OPEN ACCESS

This article is licensed under a Creative Commons Attribution 4.0 International License, which permits use, sharing, adaptation, distribution and reproduction in any medium or format, as long as you give appropriate credit to the original author(s) and the source, provide a link to the Creative Commons licence, and indicate if changes were made. The images or other third party material in this article are included in the article's Creative Commons licence, unless indicated otherwise in a credit line to the material. If material is not included in the article's Creative Commons licence and your intended use is not permitted by statutory regulation or exceeds the permitted use, you will need to obtain permission directly from the copyright holder. To view a copy of this licence, visit http://creativecommons.org/licenses/by/4.0/.

REFERENCES

1. M. Zhong, H. Sun, W. Liu, X. Zhu, and J. He: *Scripta Mater.*, 2005, vol. 53 (2), pp. 159–64.
2. B. Geddes, H. Leon, and X. Huang: *Superalloys: Alloying and Performance*, ASM International, Materials Park, 2010.
3. A. Seidel, T. Finaske, A. Straubel, H. Wendrock, T. Maiwald, M. Riede, E. Lopez, F. Brueckner, and C. Leyens: *Metall. Mater. Trans. A*, 2018, vol. 49A, pp. 3812–30.
4. L.N. Carter, K. Essa, and M.M. Attallah: *Rapid Prototyp. J.*, 2015, vol. 21 (4), pp. 423–32.
5. S. Catchpole-Smith, N. Aboulkhair, L. Parry, C. Tuck, I.A. Ashcroft, and A. Clare: *Addit. Manuf.*, 2017, vol. 15, pp. 113–22.
6. I. Todd: *Nature*, 2017, vol. 549 (7672), pp. 342–43.
7. J.H. Boswell, D. Clark, W. Li, and M.M. Attallah: *Mater. Des.*, 2019, vol. 174, p. 15.
8. H. Kazempour-Liasi, M. Tajally, and H. Abdollah-Pour: *Int. J. Miner. Metall. Mater.*, 2020, vol. 27 (6), pp. 764–73.
9. X. Wang: *Improving the Microstructure, Mechanical Properties & Process Route in Selective Laser Melting of Nickel-Superalloys*, University of Birmingham, Birmingham, 2018.
10. D. Tomus, T. Jarvis, X. Wu, J. Mei, P. Rometsch, E. Herny, J.F. Rideau, and S. Vaillant: *Phys. Proc.*, 2013, vol. 41, pp. 823–27.
11. L.N. Carter, M.M. Attallah, and R.C. Reed: *Superalloys*, 2012, vol. 2012 (6), pp. 577–86.
12. V. Juechter, T. Scharowsky, R.F. Singer, and C. Körner: *Acta Mater.*, 2014, vol. 76, pp. 252–58.
13. R. Duan, S. Li, B. Cai, Z. Tao, W. Zhu, F. Ren, and M.M. Attallah: *Compos. Part B Eng.*, 2021, vol. 222, p. 1.
14. S.A. Khairallah, A.T. Anderson, A. Rubenchik, and W.E. King: *Acta Mater.*, 2016, vol. 108, pp. 36–45.
15. V. Gunenthiram, P. Peyre, M. Schneider, M. Dal, F. Coste, I. Koutiri, and R. Fabbro: *J. Mater. Process. Technol.*, 2018, vol. 251, pp. 376–86.
16. A.B. Anwar and Q.-C. Pham: *Addit. Manuf.*, 2018, vol. 22, pp. 86–97.
17. G. Repossini, V. Laguzza, M. Grasso, and B.M. Colosimo: *Addit. Manuf.*, 2017, vol. 16, pp. 35–48.
18. R. O'Leary, R. Setchi, P. Prickett, G. Hankins, and N. Jones: *InImpact J. Innov. Impact*, 2016, vol. 8 (2), pp. 377–88.
19. H.P. Tang, M. Qian, N. Liu, X.Z. Zhang, G.Y. Yang, and J. Wang: *JOM*, 2015, vol. 67 (3), pp. 555–63.
20. L.N. Carter, X. Wang, N. Read, R. Khan, M. Aristizabal, K. Essa, and M.M. Attallah: *Mater. Sci. Technol.*, 2016, vol. 67 (3), pp. 1–5.
21. Y. Liu, J. Zhang, and Z. Pang: *Opt. Laser Technol.*, 2018, vol. 98, pp. 23–32.
22. Y.H. Zhou, Z.H. Zhang, Y.P. Wang, G. Liu, S.Y. Zhou, Y.L. Li, J. Shen, and M. Yan: *Addit. Manuf.*, 2019, vol. 25, pp. 204–17.
23. H.J. Willy, X. Li, Z. Chen, T.S. Herng, S. Chang, C.Y.A. Ong, C. Li, and J. Ding: *Mater. Des.*, 2018, vol. 157, pp. 24–34.
24. A. Hussein, L. Hao, C. Yan, and R. Everson: *Mater. Des.*, 2013, vol. 52, pp. 638–47.
25. L.N. Carter: *Selective Laser Melting of Nickel Superalloys For High Temperature Applications*, University of Birmingham, Birmingham, 2013.
26 S.S. Sih and J.W. Barlow: *Measurement and Prediction of the Thermal Conductivity of Powders at High Temperatures*, Solid Freeform Fabrication Proc, Austin, 1994.
27. F. Shen, Y. Wang, J. Yao, and J.L. Yang: *J. Sichuan Univ.*, 2005, vol. 37, pp. 47–51.

28. X. Wang, L.N. Carter, B. Pang, M.M. Attallah, and M.H. Loretto: *Acta Mater*., 2017, vol. 128, pp. 87–95.
29. X. Wang, N. Read, L.N. Carter, R.M. Ward, and M.M. Attallah: Defect Formation and Its Mitigation in Selective Laser Melting of High γ' Ni-Base Superalloys. *Superalloys 2016: Proc 13th Int. Symp. of Superalloys*, Hoboken, NJ, 2016.
30. D. Wang, S. Wu, F. Fu, S. Mai, Y. Yang, Y. Liu, and C. Song: *Mater. Des*., 2017, vol. 117, pp. 121–30.
31. Y. Liu, Y. Yang, S. Mai, D. Wang, and C. Song: *Mater. Des*., 2015, vol. 87, pp. 797–806.
32 S. Paterl, P. Reddy, and A. Kumar: *Int. J. Heat Mass Transfer*, 2021, vol. 164, p. 120575.
33 B. Dikshit, G.R. Zende, M.S. Bhatia, and B.M. Suri: *Phys. Fluids*, 2009, vol. 21 (8), p. 1196.
34. L.N. Carter, C. Martin, PJ. Withers, and M.M. Attallah: *J. Alloys Compd*., 2014, vol. 615, pp. 338–47.

Publisher's Note Springer Nature remains neutral with regard to jurisdictional claims in published maps and institutional affiliations.